Figure 1. Difficulties and resolution for use of lectin column chromatography in glycoproteomics. (A) Since detergent, high salt, and organic solvent are unusable, lectin column purification using undigested protein samples results in significant contamination of non-specific proteins due to protein-protein interactions. High concentration of eluting salt is also involved in final product. (B) When starting with digested peptide mixtures, glycopeptide enrichment yield is relatively high. However, direct analysis of eluted glycopeptides is difficult because of low ionization efficiency and impossibility of automated database search. (C) When captured glycopeptides are eluted with N-glycosidase, highly specific elution of originally glycosylated peptide could be achieved. If this reaction is combined with ^{18}O-labeling method, direct LC/MS/MS analysis can identify glycosylation sites specifically as 3 Da increased asparagine residues.

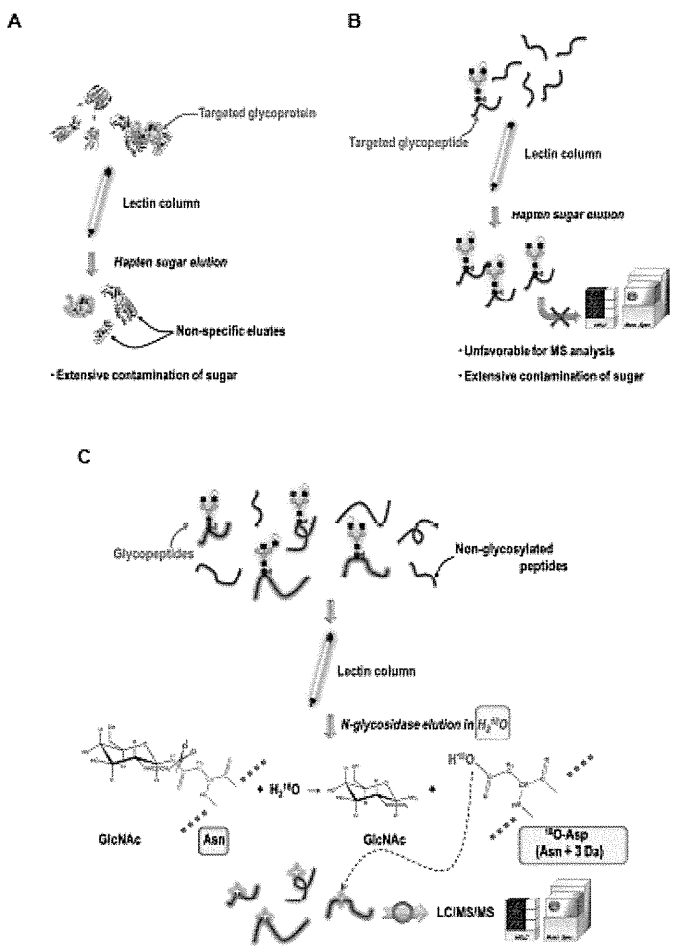

Figure 2. Representative scheme for comprehensive quantification of glycan structure alterations. Following tryptic digestion of serum samples, LC/MS/MS analysis of enriched glycopeptides and total peptides should be performed individually in order to eliminate the effect of core protein concentration variations. Finally the changing rate of glycans on each peptide could be calculated by subtracting quantification results of total peptides from those of enriched glycopeptides. The representative method for glycopeptide enrichment is IGEL technology illustrated in Fig. 1 (C).

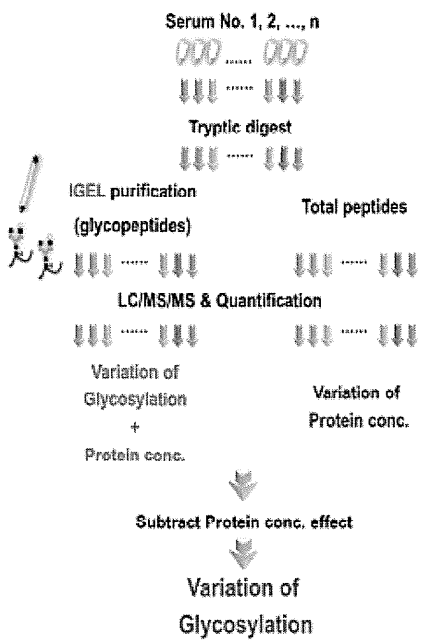

Figure 3. Principle of GalNAz-based O-glycosylated protein profiling. Metabolic incorporation of GalNAz residue at the reducing terminus of O-glycans enables subsequent capture by alkene reactive resins.

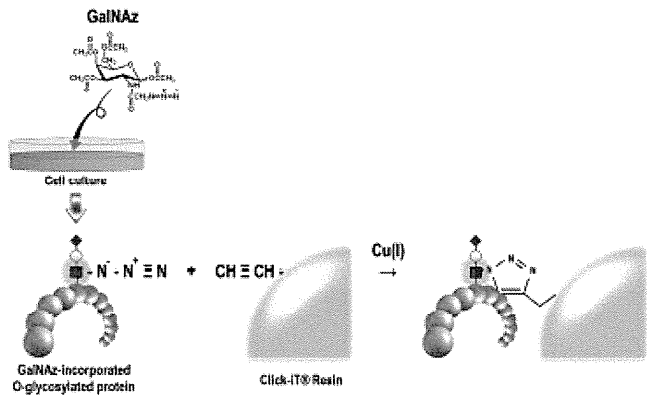

Figure 4. Quantitative evaluation of site-specific glycan structure microheterogeneities by Energy resolved oxonium ion monitoring (Erexim) technology. Representative Erexim curves for a pair of structural isomers detected on IgG molecule are shown. Six oxonium ions listed on the right side were quantitatively monitored by MRM mode. The patterns of collision energy-dependent ion yield curves for m/z = 204 and 366 were clearly distinguishable between α1,6-linked galactose (left) and α1,3-linked galactose (right) at the non-reducing termini.

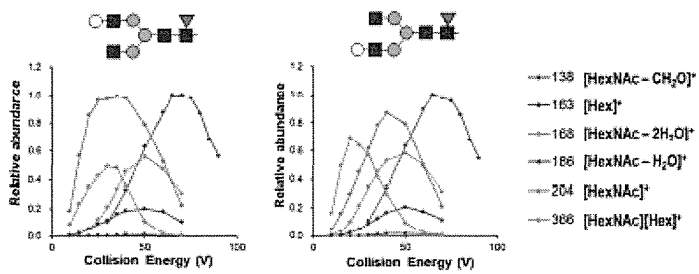

Table 1. Serum glycopeptide enrichment rate by 9 lectin columns

Lectin	Protein IDs[1]	Peptide IDs[2]	IGEL(+)[3]	IGEL(%)[4]
LCA	109	173	153	88.3
Lotus	51	27	10	36.7
SNA-I	110	194	186	95.9
SNA-II	62	57	33	57.6
UEA-I	13	13	6	46.4
WGA	82	78	41	52.4
LPA	26	14	5	35.7
ConA	183	413	388	93.9
SSA	229	519	425	81.9

[1] Number of identified proteins.

[2] Number of identified peptides.

[3] Number of peptides possessing IGEL-tags (3 Da increased asparagine residues).

[4] Ratio of IGEL-tagged peptides in total peptide identification, indicating glycopeptide enrichment rate.

Regular Article

LYMPHOID NEOPLASIA

Preapoptotic protease calpain-2 is frequently suppressed in adult T-cell leukemia

Makoto Ishihara,[1] Natsumi Araya,[2] Tomoo Sato,[2] Ayako Tatsuguchi,[1] Naomi Saichi,[1] Atae Utsunomiya,[3] Yusuke Nakamura,[4] Hidewaki Nakagawa,[1] Yoshihisa Yamano,[2] and Koji Ueda[1]

[1]Laboratory for Biomarker Development, Center of Genomic Medicine, RIKEN, Tokyo, Japan; [2]Department of Molecular Medical Science, Institute of Medical Science, St. Marianna University School of Medicine, Kawasaki, Japan; [3]Department of Hematology, Imamura Bun-in Hospital, Kagoshima, Japan; and [4]Section of Hematology/Oncology, Department of Medicine Faculty, The University of Chicago, Chicago, IL

Key Points

- Proteome-wide analysis of HTLV-1–infected T cells identified 17 biomarker proteins for the diagnosis of ATL or HAM/TSP patients.

Adult T-cell leukemia (ATL) is one of the most aggressive hematologic malignancies caused by human T-lymphotropic virus type 1 (HTLV-1) infection. The prognosis of ATL is extremely poor; however, effective strategies for diagnosis and treatment have not been established. To identify novel therapeutic targets and diagnostic markers for ATL, we employed focused proteomic profiling of the $CD4^+CD25^+CCR4^+$ T-cell subpopulation in which HTLV-1–infected cells were enriched. Comprehensive quantification of 14 064 peptides and subsequent 2-step statistical analysis using 29 cases (6 uninfected controls, 5 asymptomatic carriers, 9 HTLV-1–associated myelopathy/tropical spastic paraparesis patients, 9 ATL patients) identified 91 peptide determinants that statistically classified 4 clinical groups with an accuracy rate of 92.2% by cross-validation test. Among the identified 17 classifier proteins, α-II spectrin was drastically accumulated in infected T cells derived from ATL patients, whereas its digestive protease calpain-2 was significantly downregulated. Further cell cycle analysis and cell growth assay revealed that rescue of calpain-2 activity by overexpressing constitutively active calpain-2 (Δ_{19}CAN2) could induce remarkable cell death on ATL cells accompanied by reduction of α-II spectrin. These results support that proteomic profiling of HTLV-1–infected T cells could provide potential diagnostic biomarkers and an attractive resource of therapeutic targets for ATL. (*Blood.* 2013;0(0):1-8)

Introduction

Human T-lymphotropic virus type 1 (HTLV-1) is a human retrovirus that is the pathogenic agent of HTLV-1–associated diseases, such as adult T-cell leukemia (ATL) and HTLV-1–associated myelopathy/tropical spastic paraparesis (HAM/TSP). Recent epidemiological studies revealed that HTLV-1 is endemic mainly in Japan, the Caribbean basin, Iran, Africa, South America, and the Melanesian islands.[1] Other estimates have shown that 20 million to 30 million people worldwide are infected with HTLV-1.[2] The infection is followed by a prolonged asymptomatic phase of 20 to 30 years, and 2% to 5% of the infected individuals develop ATL during their lifetime.[3] ATL is one of the most aggressive hematologic malignancies characterized by increased numbers of lymphocytes with multilobulated nuclei, so-called flower cells, in blood circulation. The prognosis is severe with the median overall survival period and 5-year survival rate of ATL patients of 7 months and 20%, respectively.[4] Recently, humanized anti-CCR4 (KW-0761) therapeutic antibody achieved a great improvement in ATL treatment in a phase 3 study. However, the disease control rate was restricted to 50%, and long-term prognosis has yet to be known.[5] For future improvements in the management of ATL, novel biomarkers for early diagnosis are urgently needed for early therapeutic intervention.

To date, comprehensive genomic or proteomic studies using $CD4^+$ T cells have been performed for this purpose,[6-9] but reproducibility and reliability of quantification results in the discovery phase were uncertain due to the diverse individual variety of HTLV-1–infected cell contents in $CD4^+$ T cells. To overcome the etiologic variety of samples, we focused on the $CD4^+CD25^+CCR4^+$ T-cell subpopulation since Yamano et al[10] recently revealed that HTLV-1 preferentially infected $CD4^+CD25^+CCR4^+$ T cells in both ATL and HAM/TSP patients. By targeting $CD4^+CD25^+CCR4^+$ T cells, we here provide the first quantitative proteome map illustrating molecular disorders in pathogenic human T cells directly associated with the onset or progression of ATL. The comprehensive and comparative interpretation of total proteome in infected cells, especially between asymptomatic HTLV-1 carriers and ATL patients, could immediately lead to specific candidates for biomarkers and drugs.

Another challenge to emphasize in this study is our recently established proteomic profiling technologies. It is indisputable that the greater the number of clinical samples analyzed, the more confidently statistical analysis can be undertaken in order to identify diagnostic markers and druggable targets. Despite this fact, previous proteomics reports could not provide high-throughput quantitative methodologies that were sufficient for dealing with even more than 10 clinical samples, excepting a study utilizing a surface enhanced laser desorption/ionization time of flight mass spectrometer. Although the surface enhanced laser desorption/ionization time of flight method drastically improved the performance in both quantification and throughput, allowing relative quantification

Submitted August 1, 2012; accepted March 25, 2013. Prepublished online as *Blood* First Edition paper, March 28, 2013; DOI 10.1182/blood-2012-08-446922.

The online version of this article contains a data supplement.

The publication costs of this article were defrayed in part by page charge payment. Therefore, and solely to indicate this fact, this article is hereby marked "advertisement" in accordance with 18 USC section 1734.

analysis for 96 samples in several hours, at most only 250 unidentified protein peaks were detectable. In the present study, we integrated the proteomics server for the huge data set "Expressionist" (Genedata A.G., Basel, Switzerland) with high-end mass spectrometers to maximize the quality and quantity of protein catalogs transferred from mass spectrometers. We first describe the discovery phase providing a panel of novel diagnostic molecules from quantification of 14 064 peptides and identification of 4763 proteins. As the functional validation phase, we further examined the physiological potential of an identified diagnostic marker candidate, calpain-2 (CAN2), particularly concerning the association of its activity with survival or progression of ATL cells.

Materials and methods

Peripheral blood mononuclear cells (PBMCs) and cell lines

PBMCs from 6 normal donors, 5 asymptomatic carriers, and 9 HAM/TSP patients used in the screening analysis were collected in the St. Marianna University School of Medicine. Those from 9 ATL patients were collected in the Imamura Bun-in Hospital. PBMCs from 4 ATL patients used for the validation experiments were provided by the Joint Study on Predisposing Factors of ATL Development. The others from 4 HAM/TSP patients were collected in the St. Marianna University School of Medicine. The use of these human specimens in this study was approved by individual institutional ethical committees: the Ethical Committee of Yokohama Institute, RIKEN (approval code Yokohama H22-3); the Ethical Committee of St. Marianna University School of Medicine; the Institutional Review Board of Imamura Bun-in Hospital; and the Ethical Committee of the University of Tokyo (approval code 10-50). This study was conducted in accordance with the Declaration of Helsinki.

SO-4, KOB, and KK1 cells were kindly provided by Dr Yoshihisa Yamano, cultured in RPMI 1640 supplemented with 10% fetal bovine serum (Cell Culture Bioscience, Tokyo, Japan), 100 kU/L interleukin 2 (Cell Science & Technology Institute Inc., Tokyo, Japan), and 1 × antibiotic-antimycotic solution (Sigma-Aldrich, MO). Jurkat, SUP-T1, CCRF-CEM, and MOLT-3 cells were cultured in RPMI 1640 supplemented with 10% fetal bovine serum and 1 × antibiotic-antimycotic solution. All cell lines were grown at 37°C in 5% CO_2. $CD3^+CD4^+CD25^+CCR4^+$ T cells were isolated with anti-CD3-FITC (eBioscience, San Diego, CA), anti-CCR4-PE (Becton Dickinson, CA), anti-CD4-Cy7 (eBioscience), and anti-CD25-APC (eBioscience) on a Cell Sorter JSAN (Bay Bioscience, Hyogo, Japan).

Sample preparation for mass spectrometric analysis

The $CD4^+CD25^+CCR4^+$ T cells were washed with phosphate-buffered saline 3 times and lysed in denaturation buffer (8 M urea in 50 mM ammonium bicarbonate). After sonication, reduction with 5 mM tris(2-carboxyethyl) phosphine (Sigma-Aldrich) at 37°C for 30 minutes, and alkylation with 25 mM iodacetamide (Sigma-Aldrich) at room temperature for 45 minutes, lysates were digested with Trypsin GOLD (Promega, WI) with protein/enzyme ratio of 25:1 at 37°C for 12 hours. The digested peptides were desalted with Oasis HLB μElution plate (Waters, MA). The collected samples were dried up with a Vacuum Spin Drier (TAITEC Co. Ltd., Saitama, Japan) and subjected to mass spectrometric analyses.

Liquid chromatography tandem mass spectrometry (LC/MS/MS)

The digested peptides were separated on a 0.1 × 200 mm homemade C_{18} column using a 2-step linear gradient, 2% to 35% acetonitrile for 95 minutes and 35% to 95% acetonitrile for 15 minutes in 0.1% formic acid with a flow rate of 200 nL/min. The eluting peptides were analyzed with a QSTAR-Elite mass spectrometer (AB Sciex, CA) in the smart information-dependent acquisition mode of Analyst QS software 2.0 (AB Sciex). The other parameters on QSTAR-Elite were shown as follows: DP = 60, FP = 265, DP2 = 15, CAD = 5, IRD = 6, IRW = 5, curtain gas = 20, and ion spray voltage = 2000 V.

Two-dimensional (2D) LC/MS/MS

Tryptic digests of $CD4^+CD25^+CCR4^+$ T cells were dissolved in 10 mM ammonium formate in 25% acetonitrile and fractionated by a 0.2 × 250 mm monolith strong cation exchange column (GL Science, Tokyo, Japan). Peptides were eluted with an ammonium formate gradient from 10 mM to 1 M in curve = 3 mode for 70 minutes using a Prominence high-performance liquid chromatography (HPLC) system (Shimadzu Corporation, Kyoto, Japan). The eluate was fractionated into 20 fractions and analyzed individually by LTQ-Orbitrap-Velos mass spectrometer (Thermo Scientific, Bremen, Germany) accompanied with the Ultimate 3000 nano-HPLC system. The fractionated peptide samples were separated with the same gradient used in the QSTAR-Elite system described previously and analyzed by LTQ-Orbitrap-Velos acquiring a full MS scan on Fourier-transition mode with MS resolution = 60 000 and simultaneously MS/MS scans for the 20 most intense precursor ions in each MS spectrum on ion-trap mode with regular resolution. Other important parameters for LTQ-Orbitrap-Velos were as follows: capillary TemP = 250, source voltage = 2 kV, MS scan range = mass-to-charge ratio (m/z) 400 to 1600, acquire data dependent CID MS/MS for top-20 intense precursors, and dynamic exclusion enabled during 30 seconds. For protein identification, all MS/MS spectra were searched against SwissProt database version 2012_06 (20 232 human protein sequences) using SEQUEST algorithm on ProteomeDiscoverer 1.3 software (Thermo Scientific) with the following parameters: MS tolerance = 3 ppm, MS/MS tolerance = 0.8 Da, maximum missed cleavages = 2, enzyme = trypsin, taxonomy = *Homo sapiens*, fixed modification = carbamidomethylation on cysteine, and variable modification = oxidation on methionine. We accepted the protein identification satisfying the false discovery rate <1% by Percolator false discovery rate estimation algorithm on ProteomeDiscoverer.

Label-free quantification analysis

The LC/MS/MS raw data were imported into the Expressionist RefinerMS module and subjected to the following data processing and relative quantification steps. The total work flow on the RefinerMS module is shown in supplemental Figure 1 (see the *Blood* Web site). The LC/MS/MS raw data set from 29 clinical samples was displayed in 2D planes (m/z vs retention time [RT]). The chromatogram grid was applied to all planes: scan counts = 10, polynom order = 3, and RT smoothing = 0. The planes were simplified by subtracting background noises using chromatogram chemical noise subtraction: RT window = 50 scans, quantile subtraction = 50%, and RT smoothing = 3 scans. After the noise subtraction, data points with intensity <10 were clipped to zero. The RT variety among 29 planes was adjusted by chromatogram RT alignment: RT transformation window = 0.2 minutes, RT search interval = 5 minutes, m/z window = 0.1 Da, and gap penalty = 1. Peaks were detected by chromatogram summed peak detection: summation window = 5 scans, overlaP = 50, minimum peak size = 4 scans, maximum merge distance = 10 points, peak RT splitting = true, intensity profiling = max, gap/peak ratio = 1%, refinement threshold = 5, consistency threshold = 0.8, and signal/noise threshold = 1. The detected peaks were grouped into isotopic clusters derived from each molecule using 2-step chromatogram isotopic peak clustering. The first parameters were as follows: minimum charge = 1, maximum charge = 10, maximum missing peaks = 0, first allowed gap position = 3, RT window = 0.1 minute, m/z tolerance = 0.05 Da, isotope shape tolerance = 10, and minimum cluster size ration = 1.2. The second parameters were as follows: minimum charge = 1, maximum charge = 10, maximum missing peaks = 0, first allowed gap position = 3, RT window = 0.1 minute, m/z tolerance = 0.05 Da, and minimum cluster size ration = 0.6.

Expression vectors and small interfering RNA (siRNA)

For the Δ_{19}CAN2 construct, the *CAPN2* fragment was amplified with primers 5′-CATGTCGACTCCCACGAGAGGGCCATCAAGT-3′ and 5′-CATTCTAGATCAAAGTACTGAGAAACAGAGCC-3′ from pBlueBacIII *CAPN2* and cloned into pEFBOS-Myc. Prior to the overexpression experiments, we confirmed that the sequence of the inserted *CAPN2* fragment was identical to the MGC sequence (accession number BC021303). The 5-μg vector

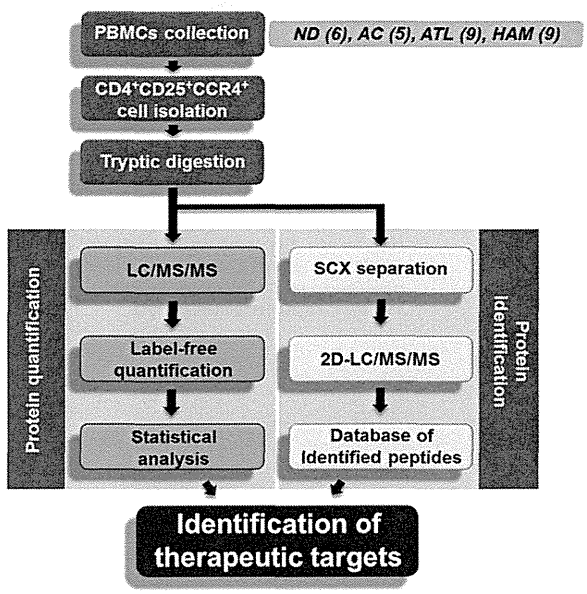

Figure 1. Schematic overview of proteomic profiling for $CD4^+CD25^+CCR4^+$ cells. PBMCs were collected from 6 normal donors, 5 asymptomatic carriers, 9 ATL patients, and 9 HAM/TSP patients, followed by isolation of the $CD4^+CD25^+CCR4^+$ subset using the cell-sorting system. The statistical candidate selection steps, including LC/MS/MS data processing, label-free quantification, and statistical analysis, were performed on the Expressionist proteome server. The protein identification database was separately established based on 2D LC/MS/MS analysis.

DNA was transfected to 1×10^6 cells. The siRNAs against *SPTAN1*, *PTMS*, *HSPE1*, and SHMT2 and siRNA universal negative control were purchased from Sigma-Aldrich. The 500-pmol siRNA oligo was transfected into 1×10^6 cells. The vectors and siRNAs were transfected into all cell lines except CCRF-CEM by Amaxa Nucleoportator transfection Kit V (Lonza, Cologne, Germany) and CCRF-CEM by Kit C (Lonza).

Cell cycle analysis and proliferation assay

For the cell cycle analysis, 1×10^5 to 2×10^5 cells were washed and agitated in 0.1% Triton-X (Sigma-Aldrich) with 100 ng/mL of ribonuclease (Sigma-Aldrich). Following addition of 1 μg/mL propidium iodide, the flow cytometric analysis was performed on FACScalibur (Becton Dickinson). The data analysis was performed using FlowJo software (Tree Star Inc., OR). Doublet events were eliminated from analyses by proper gating on FL2-W/FL2-A primary plots before histogram analysis of DNA content. Cell proliferation was estimated by measuring cell metabolic activity using Cell Counting Kit-8 (Dojindo, Kumamoto, Japan) following the manufacturer's recommendation.

Western blotting

Cells were lysed in lysis buffer [1% NP-40, 2 mM EGTA, 2 mM $MgCl_2$, 150 mM NaCl, 20 mM tris(hydroxymethyl)aminomethane–HCl (pH 7.5), 10% glycerol, containing the protease inhibitor cocktail Complete (Roche, IN, USA)] and subjected to sodium dodecyl sulfate–polyacrylamide gel electrophoresis and transferred onto PVDF membranes. Following blocking with 4% Block Ace (Yukijirushi Nyugyo Inc., Tokyo, Japan), membranes were incubated with anti-myc (9E10, Sigma-Aldrich) or anti–α-II spectrin (Abcam, Cambridge, UK) antibodies. Membranes were then incubated with horseradish peroxidase–conjugated anti-mouse IgG (GE Healthcare, NJ, USA) or anti-rabbit IgG (GE Healthcare), respectively, and visualized with Western Lightning kit (Perkin Elmer, MA).

Multiple reaction monitoring (MRM)

$CD4^+$ T cells were isolated from PBMCs using flow cytometry. The tryptic digests of the isolated cells were analyzed by 4000 Q-TRAP mass spectrometer (AB Sciex) accompanied with Ultimate 3000 nano-HPLC system. The LC gradient was as follows: 2% to 30% acetonitrile for 10 minutes and 30% to 95% acetonitrile for 5 minutes in 0.1% formic acid with a flow rate of 300 nL/min. The MRM transitions monitored were m/z 409.7/375.2 for α-II spectrin (SPTA2); m/z 538.3/889.5 for parathymosin (PTMS); m/z 507.3/147.1 for heat shock 10-kDa protein, mitochondrial (CH10); m/z 490.3/147.1 for serine hydroxymethyltransferase, mitochondrial (GLYM); and m/z 581.3/919.5 for β-actin, respectively. Individual peak areas were normalized by the peak area of β-actin. Data acquisition was performed with ion spray voltage = 2300 V, curtain gas = 10 psi, nebulizer gas = 10 psi, and an interface heating temperature = 150°C. The parameters were set as follows: declustering potential = 60, entrance potential = 10, collision cell exit potential = 10, and dwell time for each transition = 10 seconds. Collision energy was optimized to achieve maximum intensity for each MRM transition as follows: 34.03 V for m/z 409.7/175.1, 24.68 eV for m/z 538.3/889.5, 23.32 eV for m/z 507.3/147.1, 37.57 eV for m/z 490.3/147.1, and 31.58 eV for m/z 581.3/919.5.

Results

Quantitative proteome profiling of $CD4^+CD25^+CCR4^+$ T cells

A schematic overview of the screening approach is shown in Figure 1. To identify diagnostic markers expressed in HTLV-1–infected T cells, a $CD4^+CD25^+CCR4^+$ subset of PBMCs from 6 uninfected volunteers, 5 asymptomatic carriers, 9 HAM/TSP patients, and 9 ATL patients was isolated by flow cytometry (Figure 2). The averaged proportion of $CD4^+CD25^+CCR4^+$ cells in $CD4^+$ T cells from 4 clinical groups was 6.48 ± 2.46%, 13.17 ± 13.06%, 20.55 ± 10.73%, and 55.83 ± 22.40%, respectively, indicating that the occupancy of viral reservoir cells varied drastically among both pathological groups and even individuals within a group. Enrichment of the infected cells was confirmed by viral load measurement of the used samples (supplemental Figure 2). As reported previously,[10] the viral load of $CD4^+CD25^+CCR4^+$ cells (37.91 copies/100 cells on average) was ~10 times higher than that of $CD4^+CD25^-CCR4^-$ cells (4.12 copies/100 cells on average), indicating that the former cells were evidently the HTLV-1–enriched fraction. This fact strongly supports the importance of enriching pathogenic cells for rigorous quantitative biomarker discovery.

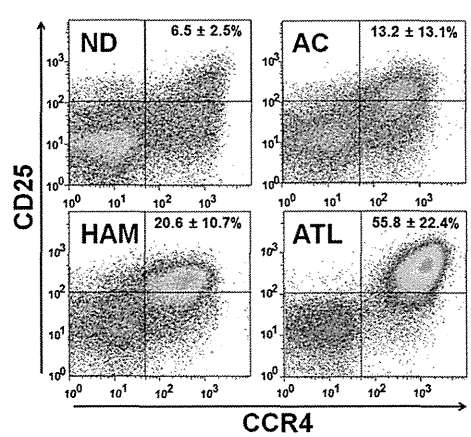

Figure 2. Representative sorting results of $CD4^+CD25^+CCR4^+$ cells. After labeling with anti-CD3-FITC, anti-CD4-Cy7, anti-CD25-APC, and anti-CCR4-PE, the $CD3^+CD4^+CD25^+CCR4^+$ fraction was isolated. The averaged content ± standard deviation (%) of $CD25^+CCR4^+$ cells out of $CD3^+CD4^+$ cells was calculated for each clinical group and is displayed in the upper right section of the panels.

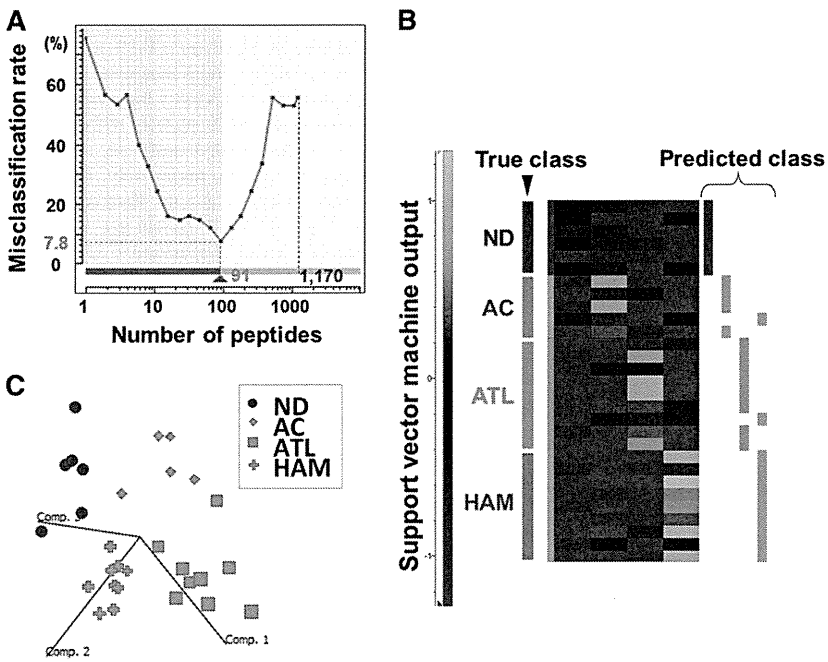

Figure 3. Statistical extraction of candidate therapeutic targets. The 14 064 nonredundant peptides detected were subjected to a 4-group Kruskal-Wallis test (ND, AC, ATL, and HAM), resulting in identification of 1170 first candidates ($P < .01$). (A) Next, the Expressionist ranking method further narrowed down the candidates to 91 peptides based on SVM-REF so that the misclassification rate in the cross-validation test became minimum, 7.8%. (B) The predicted classification result by leave-one-out cross-validation test. The 27 out of 29 cases were successfully classified into the true classes. (C) The three-dimensional plot shows the additional assessment for the classification power of 91 classifiers by principal component analysis. Comp. 1 to 3 indicate principal components 1 to 3. Q:24

An accurately adjusted number of $CD4^+CD25^+CCR4^+$ cells from 29 cases were digested with trypsin and subjected to LC/MS/MS analysis individually. Because recent mass spectrometers often deal with data on the order of hundreds of megabytes per sample, it has been considered almost impossible to calculate a data set larger than a gigabyte from large-scale clinical samples on desktop computers. Hence, we constructed a proteomics server equipped with a 12-core central processing unit, 36 SAS hard disks, and 192-GB physical memories driving the Expressionist, which was designed to combine the database module, the data processing module, and the statistical analysis module into a single integrative platform for genomics, proteomics, and metabolomics. The detailed work flow for data processing and quantification for 29 LC/MS/MS raw data was described in the "Materials and methods" and is illustrated in supplemental Figure 1. Finally, 68 454 nonredundant peaks were detected and grouped into 37 143 isotopic clusters, or molecules. As tryptic peptides should appear as multivalent ions in electrospray ionization mass spectra, 23 079 singly charged ions were removed, resulting in utilization of 14 064 peptide signals for further statistical selection of diagnostic markers.

Statistical identification of candidate diagnostic markers for ATL

A stepwise statistical extraction was employed for the effective identification of proteins, which demonstrated specific up- or downregulation in the ATL group. In the first stage, a 4-group Kruskal-Wallis test was performed to roughly extract the candidates showing a significantly distinct expression level among 4 clinical groups. Here we set the cutoff line at $P < .01$ and obtained 1170 first candidate peptides simply because the isolated peptide set using this criterion showed the best performance in the following prediction model.

Next, we selected the final candidates by the support vector machine–recursive feature elimination (SVM-RFE) algorithm in the Expressionist Analyst module. SVM-RFE is a candidate elimination method based on SVM, which enabled us to improve the classification outputs by selecting the best-performing peptide set among initially provided candidates.[11] As a result, a combination of 91 peptides showed the lowest misclassification rate (7.78%) in a leave-one-out cross-validation test (Figure 3A-B). To evaluate the classification efficiency of 91 selected candidates, the principal component analysis was performed. Figure 3C shows the three-dimensional plot of 29 clinical samples based on the 3 best-explainable components, which illustrated statistically clear segregation among the 4 clinical groups. These assessments indicated that the 91 peptides should be a sufficient set of classifiers that closely associated with the pathological characteristics of the 4 clinical groups.

Based on an independently constructed 6279-protein identification database for $CD4^+CD25^+CCR4^+$ cells using 2D LC/MS/MS (see details in "Materials and methods"), 19 peptides among the 91 candidate peptides were successfully assigned to 17 proteins listed in Table 1. The mass spectrometric quantification profiles for the 19 peptides are also shown in Figure 4 (box plots).

Recovering CAN2 activity induced cell death in ATL cells

Our diagnostic marker discovery for ATL identified an enzyme-substrate pair, CAN2 and SPTA2, which demonstrated significantly aberrant expression level in ATL patients (Figure 4). Interestingly, the intensities of the 2 proteins in 27 screening cases (without 2 statistical outliers in Figure 4) showed a clearly inverse correlation ($R^2 = 0.395$, Figure 5A). To examine whether CAN2 downregulation and/or SPTA2 upregulation might be essential for the growth of ATL cells, the enzymatic activity of CAN2 was rescued by overexpressing the constitutively active form of calpain-2 (Δ_{19}CAN2) in 3 ATL cell lines, SO-4, KOB, and KK1. After 36 hours of transfection, significant inhibition of cell proliferation (Figure 5B) and induction of sub-G1 transition was observed by activation of CAN2 in 3 ATL cells, but not in 4 non-ATL leukemia cell lines (Figure 5C). Furthermore, overexpression of Δ_{19}CAN2 drastically attenuated the expression level of SPTA2 in the ATL cell line SO-4 (Figure 5D), but not in the non-ATL leukemia cell line Jurkat (Figure 5E). On the other hand, an additional cell proliferation

Q:27 **Table 1. List of 17 protein classifiers for categorization of ND, AC, HAM/TSP, and ATL**

Accession	Protein name	*P* value (Kruskal-Wallis test)	m/z	RT	Charge	Peptide score	Identity or homology threshold	Sequence
LPPL	Eosinophil lysophospholipase	2.3.E-03	409.722	47.4	2	36.3	27	MVQVWR
CH10	Heat shock 10-kDa protein, mitochondrial	2.5.E-03	430.721	40.6	2	26.2	21	GGIMLPEK
PRG2	Bone marrow proteoglycan	2.4.E-03	528.271	64.6	2	31.6	28	RLPFICSY
MOES	Moesin	8.1.E-04	532.253	26.8	2	46.2	29	EKEELMER
MNDA	Myeloid cell nuclear differentiation antigen	9.4.E-03	647.863	69.1	2	67.3	24	SLLAYDLGLTTK
GLYM	Serine hydroxymethyltransferase, mitochondrial	8.7.E-04	408.551	21.6	3	31.1	18	HADIVTTTTHK
PTMS	Parathymosin	9.7.E-04	453.875	17.8	3	41.2	25	AAEEEDEADPKR
TPIS	Triosephosphate isomerase	9.1.E-03	472.266	71.0	3	54.0	28	QSLGELIGTLNAAK
HSP71	Heat shock 70-kDa protein 1A/1B	9.7.E-03	563.307	65.5	3	93.8	21	IINEPTAAAIAYGLDR
CD6	T-cell differentiation antigen CD6	7.7.E-03	592.306	37.8	3	62.7	22	VLCQSLGCGTAVERPK
ANXA1	Annexin A1	4.4.E-04	612.347	61.5	3	57.0	17	RKGTDVNVFNTILTTR
ANXA6	Annexin A6	2.3.E-03	669.017	70.9	3	54.7	16	AMEGAGTDEKALIEILATR
SPTA2	Spectrin α chain, brain	5.4.E-03	409.718	28.8	2	42.7	30	EAGSVSLR
GLYM	Serine hydroxymethyltransferase, mitochondrial	1.1.E-03	428.240	57.0	2	42.8	27	SGLIFYR
DRB1s	HLA class II histocompatibility antigen, DRB1-1, 4, 10, 11, 13, 15, 16 β chain	1.0.E-02	478.216	25.8	2	55.9	25	AAVDTYCR
CAN2	Calpain-2 catalytic subunit	2.4.E-03	483.253	54.0	2	66.6	29	SDTFINLR
STAT1	Signal transducer and activator of transcription 1-α/β	7.3.E-03	486.290	21.7	2	39.1	29	KILENAQR
PRG2	Bone marrow proteoglycan	9.4.E-04	497.742	49.2	2	31.6	27	FQWVDGSR
CXCL7	Platelet basic protein	1.3.E-03	528.761	43.1	2	51.7	28	ICLDPDAPR

assay using siRNA against *SPTAN1* revealed that reduction of SPTA2 was not sufficient for the induction of cell death for ATL cells (supplemental Figures 3 and 4).

In addition, 3 proteins (PTMS, CH10, and GLYM) were also found to be upregulated in ATL cells. To address the roles of these proteins, a cell proliferation assay was conducted using 3 ATL cell lines treated with siRNAs against *PTMS*, *HSPE1* (gene symbol of CH10), or *SHMT2* (gene symbol of GLYM) (supplemental Figure 4). As a result, suppression of the *SHMT2* gene induced significant growth inhibition for all 3 ATL cell lines. Although si*HSPE1*-treated KOB cells showed a statistically significant decrease in cell growth rate, si*HSPE1* and si*PTMS* had only partial or no effects on proliferation of ATL cell lines. To further confirm whether the overexpression of SPTA2, PTMS, CH10, or GLYM

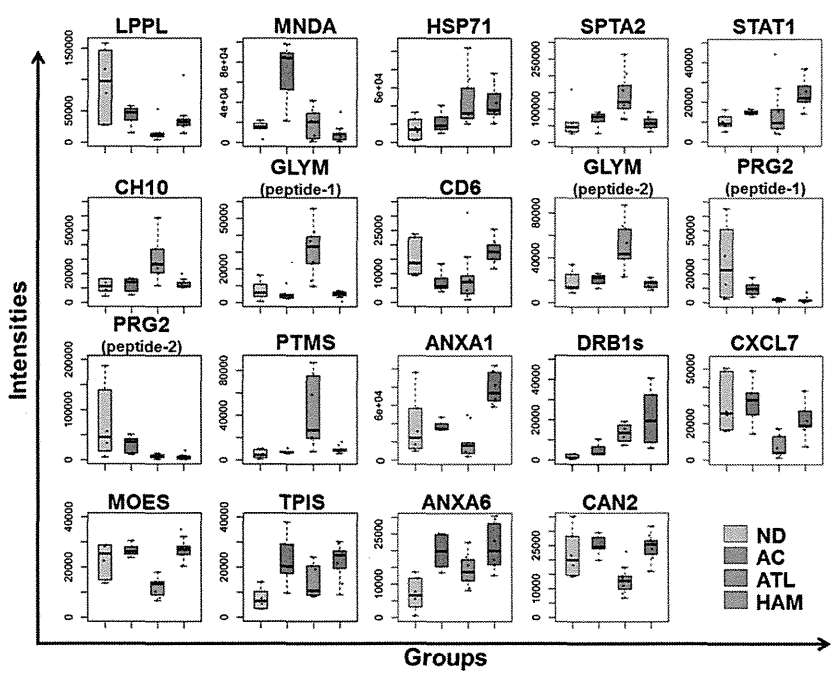

Figure 4. Summary of quantitative features for the 17 protein classifiers identified. The 19 box plots (see Table 1 for protein names) show the results of mass spectrometric quantification and protein identification. We finally identified 19 peptides out of 91 candidates in Figure 3, which were assigned to 17 proteins. Proteins identified from 2 distinct peptides were shown as GLYM (peptides 1 and 2) or PRG2 (peptides 1 and 2). The y-axis indicates normalized relative intensity of peptides in mass spectrometric data.

Q:25

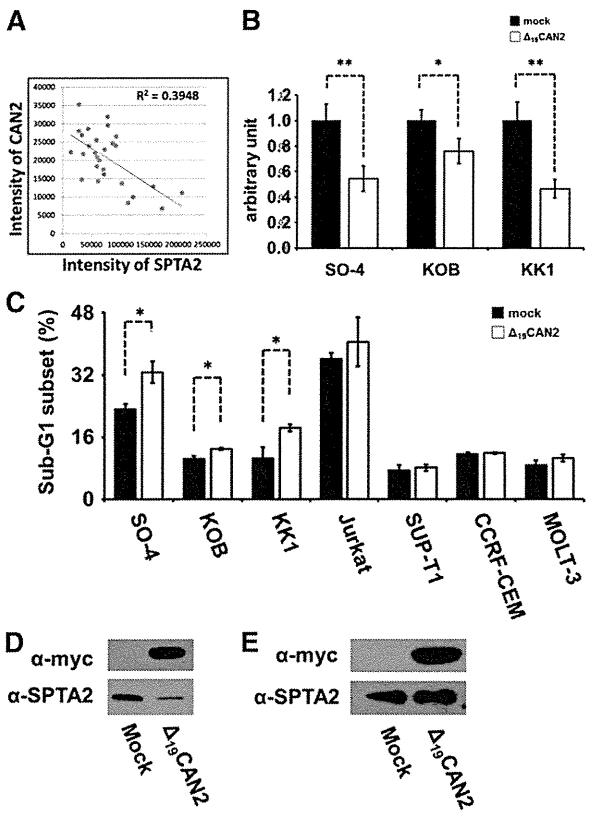

Figure 5. Rescue of CAN2 activity induced cell death in ATL cells. (A) Correlation between CAN2 and SPTA2 expression level in 27 cases. (B) Cell proliferation was measured by MTT assay on SO-4, KOB, and KK1 cells 36 hours after transfection of mock vector or Δ_{19}CAN2. $^{*}P < .05$; $^{**}P < .01$ by Student *t* test. (C) Overexpression of Δ_{19}CAN2 significantly accelerated cell death in 3 ATL (SO-4, KOB, and KK1) and 4 non-ATL (Jurkat, SUP-T1, CCRF-CEM, and MOLT-3) cell lines. $^{**}P < .05$ by Student *t* test. The drastic attenuation of SPTA2 expression was observed after transfection of Δ_{19}CAN2 in SO-4 cells (D), but not in Jurkat cells (E). The immunoblot of anti-myc tag confirmed the expression of exogenous Δ_{19}CAN2.

protein would be an ATL-specific molecular signature, the expression levels of these proteins in 8 clinical samples were evaluated by the mass spectrometric quantification technology MRM (supplemental Figures 5 and 6). Expression of SPTA2, GLYM, and CH10 in cells derived from ATL patients was significantly higher than that in cells derived from HAM/TSP patients. The level of PTMS also showed a clearly increasing tendency in the ATL patient group. Taken together, these results suggested that the deprivation of CAN2 activity and upregulation of GLYM in HTLV-1–infected T cells might have a key role at the onset or progression of ATL.

Discussion

In the past decade, proteomics technologies have developed dramatically for the purpose of obtaining more and more comprehensive and sensitive proteome maps in cells or clinical specimens. The performance of mass spectrometers in particular has exhibited remarkable progress; however, as for sensitivity and throughput, it has still been difficult to identify biomarkers from crude samples including body fluids or total cell lysate. A major reason could be that the range of protein concentration in the analyte is indeed much larger than the dynamic range of recent mass spectrometers.[12] The other essential factor to be improved for clinical proteomics is the capacity of the bioinformatics platform to allow analysis of a sufficient number of clinical samples in order to statistically overcome the significant individual variability.[13]

Concerning the first issue, we previously developed and applied various focused proteomic applications targeting molecular biochemical features including glycan structure biomarkers[14-16] and low-molecular-weight peptide biomarkers.[17] The preenrichment of subproteome fractions effectively reduces the complexity of crude samples and allowed us to identify potential serum cancer biomarkers successfully. Through our previous knowledge, we provide an approach for investigating infectious diseases by employing virus-infected cell-focused proteomics. In addition to HTLV-1, for instance, isolation of HIV-infected cells is highly desired because the frequency of these cells in AIDS patients' PBMCs is ~1 out of 10^4 to 10^5 cells.[18] Actually, we successfully demonstrated the effect of HTLV-1–infected cell isolation on the elimination of individual variability (Figure 2, supplemental Figure 2) and reliable identification of disease state–associated proteins (Figures 4 and 5). We further showed the potential of the next-generation bioinformatics platform Expressionist to remove the constraint on the capacity of data size acquired from high-end mass spectrometers. Expressionist covered whole discovery steps from processing of raw mass spectrometer data to statistical analyses (Figures 1 and 3, and supplemental Figure 1) and, importantly, could perform quantification analysis using a basically unlimited number of clinical samples. Hence, in parallel with the development of mass spectrometers, high-spec and inexpensive OMICS server systems are necessary for future diagnostic marker and therapeutic target discoveries using hundreds or thousands of clinical specimens.

In this study, we focused on the $CD4^+CD25^+CCR4^+$ T-cell subpopulation in which T helper 2, T helper 17, and regulatory T (Treg) cells were mainly involved.[10] The purpose for which we used this subset was to technically enrich the preferential viral reservoir cells and to strengthen reliability of screening results. However, investigating proteome behaviors of these subtypes in HTLV-1–associated diseases is also important physiologically because it has been frequently reported that deregulated Treg plays significant roles in pathogenesis of ATL and HAM/TSP. Indeed, aberrant proliferation of Treg cells is considered the main cause of immunodeficiency in ATL patients because of their innate immunosuppressive functions,[19] whereas abnormal production of interferon γ from infected Treg cells might induce chronic spinal inflammation in HAM/TSP patients.[20] Given the list of our 17 classifier proteins, activation of signal transducer and activator of transcription 1-α/β is the well-known key factor for HAM/TSP,[21] whereas upregulation of heat shock 70-kDa protein 1A/1B, CH10, and PTMS were reported in many other types of tumors.[22-24] The association of these 4 proteins with the etiology of HAM/TSP and ATL would be evident according to the previous work, supporting that our other candidates might similarly have a direct impact on the transformation of Treg cells after infection of HTLV-1. Particularly, the specific upregulation of GLYM in ATL cells represents the first evidence that excessive folate metabolism might be essential for the progression or survival of ATL cells because GLYM is a fundamental enzyme catalyzing the supply of glycine accompanying the conversion of tetrahydrofolate to 5,10-methylenetetrahydrofolate.[25] Indeed, the suppression of GLYM expression, which was confirmed to be upregulated in ATL patients, resulted in significant reduction of cell growth. This observation suggests that diminishing GLYM expression or enzyme activity could be a promising strategy for

molecular-targeting treatment of ATL. Together with the downregulation of CAN2 in the ATL cells shown in Figure 5, the proteins listed in Table 1 could provide the molecular basis for not only interpretation of physiological mechanisms in ATL or HAM/TSP but also development of novel therapeutic agents for HTLV-1–associated diseases.

CAN2 belongs to a Ca^{2+}-regulated cytosolic cysteine protease family, which includes 14 calpain isoforms.[26] The enzymatic activity of calpain is implicated in diverse physiological processes, such as cytoskeletal remodeling, cellular signaling, and apoptosis.[26] As an example of a spectrin-mediated apoptosis pathway, it was reported that CAN2 produced SPTA2 breakdown products following traumatic brain injury.[27] Because SPTA2 interacts with calmodulin and constructs the membrane cytoskeletons, its breakdown is considered a process of membrane structural changes during cell death.[28,29] This fact is concordant with our finding in ATL, suggesting that accumulation of SPTA2 in ATL cells can be attributed to the suppression of CAN2 expression and contribute to circumvent apoptosis. In the analysis of basal levels of CAN2 and SPTA2 in 7 cell lines (supplemental Figure 7), 3 ATL cell lines showed endogenous expression of CAN2 and moderate levels of SPTA2. On the other hand, 4 non-ATL leukemia cells demonstrated very high expression of SPTA2 and undetectable levels of CAN2. Although we found the downregulation of CAN2 and accumulation of SPTA2 in ATL cells, this tendency might be more distinctive in HTLV-1 (–) leukemia cells. Taken together, even though the expression level of CAN2 was indeed suppressed in ATL cells, the CAN2-SPTA2 apoptotic pathway itself might remain normal. In contrast, this pathway was considered to be impaired at multiple stages in HTLV-1 (–) leukemia cells because CAN2 expression was completely diminished (supplemental Figure 7) and overexpression of CAN2 could not reactivate the CAN2-SPTA2 apoptotic pathway (Figure 5B-E). In these cells, not only genetic downregulation of CAN2 but also inhibition of CAN2 enzymatic activity might be involved in the carcinogenesis.

In conclusion, comprehensive proteomic profiling of HTLV-1–infected T cells provided 17 disease-associated signature proteins, which have great potential for future clinical use as diagnostic biomarkers. As we described regarding the relationship between the CAN2-SPTA2 pathway and ATL phenotypes, further individual functional analyses will contribute to understanding the detailed molecular mechanisms involved in the onset or progression of HAM/TSP and ATL.

Acknowledgments

The authors thank Dr Hiroyuki Sorimachi for kindly providing pBlueBacIIICAPN2 vector.

This work was supported by Research on Measures for Intractable Diseases, the Ministry of Health Labour and Welfare Japan.

Authorship

Contribution: M.I. and K.U. designed the study, performed experiments, analyzed results, and wrote the manuscript; A.T. and N.S. performed experiments; N.A., T.S., A.U., and Y.Y. collected the clinical samples and performed flow cytometric experiments; Y.N. and H.N. revised the manuscript; and all authors discussed the results and commented on the manuscript.

Conflict-of-interest disclosure: The authors declare no competing financial interests.

Correspondence: Koji Ueda, Laboratory for Biomarker Development, Center for Genomic Medicine, RIKEN, General Research Building 6F, Institute of Medical Science, 4-6-1 Shirokanedai, Minato-ku, Tokyo, Japan, 1088639; e-mail: k-ueda@riken.jp. Q:20

References

1. Yamashita M, Ido E, Miura T, Hayami M. Molecular epidemiology of HTLV-I in the world. *J Acquir Immune Defic Syndr Hum Retrovirol.* 1996;13(suppl 1):S124-S131.
2. Asquith B, Zhang Y, Mosley AJ, et al. In vivo T lymphocyte dynamics in humans and the impact of human T-lymphotropic virus 1 infection. *Proc Natl Acad Sci U S A.* 2007;104(19):8035-8040.
3. Sakashita A, Hattori T, Miller CW, et al. Mutations of the p53 gene in adult T-cell leukemia. *Blood.* 1992;79(2):477-480.
4. Beltran B, Quiñones P, Morales D, Cotrina E, Castillo JJ. Different prognostic factors for survival in acute and lymphomatous adult T-cell leukemia/lymphoma. *Leuk Res.* 2011;35(3):334-339.
5. Ishida T, Joh T, Uike N, et al. Defucosylated anti-CCR4 monoclonal antibody (KW-0761) for relapsed adult T-cell leukemia-lymphoma: a multicenter phase II study. *J Clin Oncol.* 2012;30(8):837-842.
6. Semmes OJ, Cazares LH, Ward MD, et al. Discrete serum protein signatures discriminate between human retrovirus-associated hematologic and neurologic disease. *Leukemia.* 2005;19(7):1229-1238.
7. Kirk PD, Witkover A, Courtney A, et al. Plasma proteome analysis in HTLV-1-associated myelopathy/tropical spastic paraparesis. *Retrovirology.* 2011;8:81.
8. Rahman S, Quann K, Pandya D, Singh S, Khan ZK, Jain P. HTLV-1 Tax mediated downregulation of miRNAs associated with chromatin remodeling factors in T cells with stably integrated viral promoter. *PLoS ONE.* 2012;7(4):e34490.
9. Polakowski N, Gregory H, Mesnard JM, Lemasson I. Expression of a protein involved in bone resorption, Dkk1, is activated by HTLV-1 bZIP factor through its activation domain. *Retrovirology.* 2010;7:61.
10. Yamano Y, Araya N, Sato T, et al. Abnormally high levels of virus-infected IFN-gamma+ CCR4+ CD4+ CD25+ T cells in a retrovirus-associated neuroinflammatory disorder. *PLoS ONE.* 2009;4(8):e6517.
11. Oh JH, Gao J, Nandi A, Gurnani P, Knowles L, Schorge J. Diagnosis of early relapse in ovarian cancer using serum proteomic profiling. *Genome Inform.* 2005;16(2):195-204.
12. Anderson NL, Anderson NG. The human plasma proteome: history, character, and diagnostic prospects. *Mol Cell Proteomics.* 2002;1(11):845-867.
13. Nordon IM, Brar R, Hinchliffe RJ, Cockerill G, Thompson MM. Proteomics and pitfalls in the search for potential biomarkers of abdominal aortic aneurysms. *Vascular.* 2010;18(5):264-268.
14. Ueda K, Katagiri T, Shimada T, et al. Comparative profiling of serum glycoproteome by sequential purification of glycoproteins and 2-nitrobenzensulfenyl (NBS) stable isotope labeling: a new approach for the novel biomarker discovery for cancer. *J Proteome Res.* 2007;6(9):3475-3483.
15. Ueda K, Fukase Y, Katagiri T, et al. Targeted serum glycoproteomics for the discovery of lung cancer-associated glycosylation disorders using lectin-coupled ProteinChip arrays. *Proteomics.* 2009;9(8):2182-2192.
16. Ueda K, Takami S, Saichi N, et al. Development of serum glycoproteomic profiling technique; simultaneous identification of glycosylation sites and site-specific quantification of glycan structure changes. *Mol Cell Proteomics.* 2010;9(9):1819-1828.
17. Ueda K, Saichi N, Takami S, et al. A comprehensive peptidome profiling technology for the identification of early detection biomarkers for lung adenocarcinoma. *PLoS ONE.* 2011;6(4):e18567.
18. Bahbouhi B, al-Harthi L. Enriching for HIV-infected cells using anti-gp41 antibodies indirectly conjugated to magnetic microbeads. *Biotechniques.* 2004;36(1):139-147.
19. Matsubar Y, Hori T, Morita R, Sakaguchi S, Uchiyama T. Delineation of immunoregulatory properties of adult T-cell leukemia cells. *Int J Hematol.* 2006;84(1):63-69.
20. Best I, López G, Verdonck K, et al. IFN-gamma production in response to Tax 161-233, and frequency of CD4+ Foxp3+ and Lin HLA-DRhigh CD123+ cells, discriminate HAM/TSP patients from asymptomatic HTLV-1-carriers in a Peruvian population. *Immunology.* 2009;128(1, pt 2):e777-e786. Q:21

21. Nakamura N, Fujii M, Tsukahara T, et al. Human T-cell leukemia virus type 1 Tax protein induces the expression of STAT1 and STAT5 genes in T-cells. *Oncogene.* 1999;18(17):2667-2675.

22. Alaiya AA, Al-Mohanna M, Aslam M, et al. Proteomics-based signature for human benign prostate hyperplasia and prostate adenocarcinoma. *Int J Oncol.* 2011;38(4):1047-1057.

23. Cappello F, Rappa F, David S, Anzalone R, Zummo G. Immunohistochemical evaluation of PCNA, p53, HSP60, HSP10 and MUC-2 presence and expression in prostate carcinogenesis. *Anticancer Res.* 2003;23(2B):1325-1331.

24. Letsas KP, Vartholomatos G, Tsepi C, Tsatsoulis A, Frangou-Lazaridis M. Fine-needle aspiration biopsy-RT-PCR expression analysis of prothymosin alpha and parathymosin in thyroid: novel proliferation markers? *Neoplasma.* 2007;54(1):57-62.

25. Anderson DD, Quintero CM, Stover PJ. Identification of a de novo thymidylate biosynthesis pathway in mammalian mitochondria. *Proc Natl Acad Sci USA.* 2011; 108(37):15163-15168.

26. Storr SJ, Carragher NO, Frame MC, Parr T, Martin SG. The calpain system and cancer. *Nat Rev Cancer.* 2011;11(5):364-374.

27. Liu MC, Akle V, Zheng W, et al. Comparing calpain- and caspase-3-mediated degradation patterns in traumatic brain injury by differential proteome analysis. *Biochem J.* 2006;394(pt 3): 715-725.

28. Wallis CJ, Wenegieme EF, Babitch JA. Characterization of calcium binding to brain spectrin. *J Biol Chem.* 1992;267(7): 4333-4337.

29. Liu X, Van Vleet T, Schnellmann RG. The role of calpain in oncotic cell death. *Annu Rev Pharmacol Toxicol.* 2004;44: 349-370.

THE JOURNAL OF BIOLOGICAL CHEMISTRY VOL. 288, NO. 9, pp. 6053–6062, March 1, 2013

Lysyl 5-Hydroxylation, a Novel Histone Modification, by Jumonji Domain Containing 6 (JMJD6)*

Received for publication, November 3, 2012, and in revised form, January 8, 2013 Published, JBC Papers in Press, January 9, 2013, DOI 10.1074/jbc.M112.433284

Motoko Unoki[‡§1], Akiko Masuda[¶], Naoshi Dohmae[¶], Kyohei Arita[‖], Masanori Yoshimatsu[**], Yukiko Iwai[‡‡], Yoshinori Fukui[‡‡], Koji Ueda[§], Ryuji Hamamoto[§§], Masahiro Shirakawa[**], Hiroyuki Sasaki[‡], and Yusuke Nakamura[**§§]**

From the [‡]Division of Epigenetics, Department of Molecular Genetics, Medical Institute of Bioregulation, Kyushu University, Fukuoka 812-8582, Japan, the [§]Laboratory for Biomarker Development, The Institute of Physical and Chemical Research, Center for Genomic Medicine, RIKEN, Tokyo 108-8639, Japan, the [¶]Biomolecular Characterization Team, RIKEN, Saitama 351-0198, Japan, the [‖]Graduate School of Engineering, Kyoto University, Kyoto 615-8510, Japan, the [**]Laboratory of Molecular Medicine, Human Genome Center, Institute of Medical Science, The University of Tokyo, Tokyo 108-8639, Japan, the [‡‡]Division of Immunogenetics, Department of Immunobiology and Neuroscience, Medical Institute of Bioregulation, Kyushu University, Fukuoka 812-8582, Japan, and the [§§]Section of Hematology/Oncology, Center for Personalized Therapeutics, The University of Chicago, Chicago, Illinois 60637

Background: JMJD6 hydroxylates U2AF65, but its role in histone modification has been obscure.
Results: Our analysis of histones purified from JMJD6 knock-out mouse embryos reveals that JMJD6 hydroxylates histone lysyl residues.
Conclusion: JMJD6 mediates histone lysyl 5-hydroxylation, which is a novel histone modification.
Significance: Our study identifies a new function for Jumonji family proteins in epigenetic modification of histones.

JMJD6 is reported to hydroxylate lysyl residues of a splicing factor, U2AF65. In this study, we found that JMJD6 hydroxylates histone lysyl residues. *In vitro* experiments showed that JMJD6 has a binding affinity to histone proteins and hydroxylates multiple lysyl residues of histone H3 and H4 tails. Using JMJD6 knock-out mouse embryos, we revealed that JMJD6 hydroxylates lysyl residues of histones H2A/H2B and H3/H4 *in vivo* by amino acid composition analysis. 5-Hydroxylysine was detected at the highest level in histones purified from murine testis, which expressed JMJD6 at a significantly high level among various tissues examined, and JMJD6 overexpression increased the amount of 5-hydroxylysine in histones in human embryonic kidney 293 cells. These results indicate that histones are additional substrates of JMJD6 *in vivo*. Because 5-hydroxylation of lysyl residues inhibited *N*-acetylation and *N*-methylation by an acetyltransferase and a methyltransferase, respectively, *in vitro*, histone 5-hydroxylation may have important roles in epigenetic regulation of gene transcription or chromosomal rearrangement.

Jumonji domain containing 6 (JMJD6),[2] which possesses high binding affinity to single-stranded RNA, is reported to hydroxylate lysyl residues of an RNA splicing factor, U2AF65 (1, 2). JMJD6 contains a JmjC domain that catalyzes lysyl hydroxylation of proteins in the presence of 2-oxoglutarate, Fe(II), and ascorbate. Proteins belonging to the JmjC family are classified into 2-oxoglutarate oxygenases (3). Among the known 2-oxoglutarate oxygenases, PLOD3 (procollagen-lysine, 2-oxoglutarate 5-dioxygenase 3) mediates hydroxylation of unmodified lysyl residues, yielding 5-hydroxylysine (4). Most JmjC family members catalyze hydroxylation of *N*-methyl groups at the ϵ-amino group of lysyl residues and generate hydroxymethyl groups, which are immediately processed to formaldehyde molecules, resulting in demethylation of methylated lysyl residues (5). However, JMJD6 does not add a hydroxyl group to the *N*-methyl group but adds it to one of the backbone carbons in a lysyl side chain and generates a stable 5-hydroxylysine (1). JMJD6 knock-out mice exhibited severe anemia, growth retardation, and a delay in terminal differentiation of the kidney, intestine, liver, and lung during embryogenesis, resulting in perinatal lethality (6, 7).

In this study, we first identified JMJD6 as a novel UHRF1 (ubiquitin-like with PHD and RING finger domains 1) interacting protein. UHRF1 has important roles in transferring DNA methylation status and recognizes histone modification status (8). Therefore, we thought that JMJD6 might hydroxylate histone molecules through interaction with UHRF1. Using JMJD6 knock-out mice, we revealed that JMJD6 hydroxylates histone lysyl residues and generates 5-hydroxylysine *in vivo*. 5-Hydroxylation is a novel histone lysyl modification. Because it interfered with *N*-acetylation and *N*-methylation by an acetyltransferase and a methyltransferase, respectively, the modification may regulate transcription through these interactions with other histone modifications.

EXPERIMENTAL PROCEDURES

JMJD6 Wild-type and Knock-out Mice—Details of the JMJD6 knock-out mice were described elsewhere (6). C57BL/6 mice

* This work was supported by JSPS KAKENHI Grant 22700867 and Kyushu University interdisciplinary programs in education and projects in research development.
[1] To whom correspondence should be addressed: Div. of Epigenetics, Dept. of Molecular Genetics, Medical Institute of Bioregulation, Kyushu University, 3-1-1 Maidashi, Higashi-ku, Fukuoka-shi, Fukuoka 812-8582, Japan. Tel.: 81-92-642-6760; Fax: 81-92-642-6799; E-mail: unokim@bioreg.kyushu-u.ac.jp.
[2] The abbreviations used are: JMJD6, Jumonji domain containing 6; qRT-PCR, quantitative RT-PCR; HAT, histone acetyltransferase; E14.5, embryonic day 14.5; AdoMet, *S*-adenosyl-L-methionine.

were used as wild-type control mice. JMJD6 knock-out embryonic day 14.5 (E14.5) embryos were obtained by crossing heterozygous JMJD6 mutant mice.

Antibodies, Plasmids, and Cell Lines—The following antibodies were used: anti-JMJD6 rabbit polyclonal antibody (ab10526, Abcam), and anti-β-actin mouse monoclonal antibody (GTX26276, GeneTex). Human *JMJD6* cDNA was cloned into pGEX-6p-1 (GE Healthcare) and pcDNA5/FRT/TO (Invitrogen). Doxycycline (Dox)-inducible JMJD6 stable cells were generated using the Flp-In T-REx system (Invitrogen) according to the manufacturer's instructions. JMJD6 expression was induced by Dox (final concentration, 0.5 μg/ml; TaKaRa, Tokyo, Japan). J1 mouse ES cells were obtained from ATCC (Manassas, VA) and maintained in DMEM with 15% fetal bovine serum (FBS), nonessential amino acids, 2-mercaptoethanol, and leukemia inhibitory factor. Flp-In T-Rex 293 cells were obtained from Invitrogen and the Dox-inducible JMJD6 stable 293 cells were maintained in DMEM with 10% FBS, 10% tetracycline-free FBS, hygromycin B (100 μg/ml), and blasticidin S (15 μg/ml).

Quantitative RT-PCR—For qRT-PCR reactions, specific primers and probes for mouse JMJD6 (forward, 5′-GACCCGGCACAACTACTACG-3′; reverse, 5′-CTCTTGTGCATTGAGCAGAAC-3′) and mouse GAPDH (forward, 5′-CCATGTTTGTGATGGGTGTG-3′ and reverse, 5′-ACTGTGGTCATGAGCCCTTC-3′) were used. PCR reactions were performed using the TaKaRa Thermal Cycler Dice® Real Time System Single following the manufacturer's instructions. Amplification conditions were 30 s at 95 °C and then 40 cycles each consisting of 5 s at 95 °C and 30 s at 60 °C.

Purification of GST-JMJD6 and in Vitro Binding Assay—Recombinant GST-JMJD6 was expressed in BL21-CodonPlus DE3-RIL cells. The transformed bacteria were incubated in L-Broth media with 0.1 mM isopropyl 1-thio-β-D-galactopyranoside at 16 °C overnight. Following this, the bacteria were lysed in sonication buffer (150 mM NaCl, 20 mM Tris-HCl (pH 7.5), 2 mM EDTA, 10% glycerol, 1% Triton X, and 0.8 mg/ml lysozyme) by sonication. GST-JMJD6 was purified using glutathione-Sepharose 4FF (GE Healthcare) and eluted by glutathione. The purified proteins were incubated with biotin-labeled histone $H3_{1-21}$ peptides (12–405, Millipore, Billerica, MA) or recombinant full-length histone H4 (14–697, Millipore) in 0.1% Nonidet P-40 lysis buffer (150 mM NaCl, 0.1% Nonidet P-40, and 50 mM Tris-HCl (pH 8.0)) for 1 h at 4 °C. The biotin-labeled histone $H3_{1-21}$ peptides were pulled down with interacting proteins by streptavidin Sepharose (S951, Invitrogen). Full-length histone H4 was immunoprecipitated with anti-JMJD6 rabbit polyclonal antibody (ab10526, Abcam), which was also used for Western blotting.

In Vitro Hydroxylation Assay—To perform the enzyme assay, GST-JMJD6 was prepared as described above. Extracted GST-JMJD6 was concentrated using a 50 K column (Millipore), and its buffer was replaced with 50 mM Tris-HCl (pH 7.5) by dialysis using EasySep (TOMY, Tokyo, JAPAN). Purity of GST-JMJD6 was assessed by Coomassie Brilliant Blue staining. The enzyme assay was performed in 50 mM Tris-HCl (pH 7.5) buffer containing 500 μM α-ketoglutarate, 100 μM L-ascorbate, 100 μM $Fe(NH_4)_2SO_4$, 10 μM GST-JMJD6, and 20 μM histone peptides.

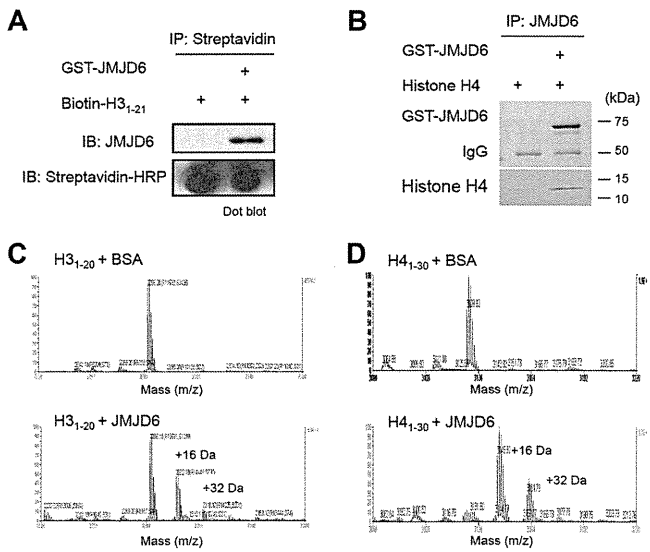

FIGURE 1. **JMJD6 interacts with and hydroxylates histone H3 and H4 *in vitro*.** *A* and *B*, *in vitro* pulldown assay. Biotin-labeled histone $H3_{1-21}$ peptides (*A*) or recombinant histone H4 (*B*) were incubated with or without GST-JMJD6, pulled down by streptavidin-Sepharose, and detected by dot blot using streptavidin-HRP (*A*) or Coomassie Brilliant Blue (*CBB*) staining (*B*). Pulled down GST-JMJD6 was detected by Western blotting using anti-JMJD6 antibody (*A*) or Coomassie Brilliant Blue staining (*B*). *C* and *D*, enzymatic activity of GST-JMJD6 was measured by MS analysis. Histone $H3_{1-20}$ (*C*) and $H4_{1-30}$ (*D*) peptides were served as substrates. BSA was used as a negative control. *IB*, immunoblot.

Protein purification and the enzyme assay were performed on the same day to avoid reduction of enzymatic activity of JMJD6.

MS Analysis—Peptides treated with JMJD6 were acidified with trifluoroacetic acid (TFA; final concentration, 0.5%) and absorbed with ZipTipC18. The captured peptides were washed with 0.1% TFA with 2% acetonitrile once and eluted with 0.5 μl of the matrix solution (4 mg/ml cyano-4-hydroxycinnamic acid, 0.1% TFA, 70% acetonitrile) onto the MALDI target plate (AB Sciex, Foster City, CA). The spotted samples were analyzed with the reflectron mode of 4800 plus MALDI-TOF-TOF mass spectrometer (AB Sciex).

Purification of Histones and Detection of 5-Hydroxylysine by Amino Acid Composition Analysis—Histones H2A/H2B and H3/H4 were separately purified from tissues or culturing cells using a histone purification kit (Active Motif, Carlsbad, CA) according to the manufacturer's instructions. The extracted histones were separated by SDS-PAGE, transferred to a membrane (Immobilon-P^{SQ}, Millipore), and stained by Coomassie Brilliant Blue. The transferred histones were used for amino acid composition analysis to detect 5-hydroxylysine.

The JMJD6-treated peptides or the purified histones were hydrolyzed in 6 N HCl vapor at 110 °C for 20 h. The acid hydrolysates of the peptides were derivatized with 6-aminoquinolyl-*N*-hydroxysuccinimidyl carbamate, and 6-aminoquinolylcarbamyl amino acid thus obtained was quantified by ion-pair chromatography using tetramethylammonium bromide on a C18-reversed phase column (L-column 2, 3.0 mm, inner diameter × 250 mm, 3 μm, CERI, Tokyo, Japan) (9). Each amino acid was separated by HPLC. The acid hydrolysates of the histones were purified on a graphitic carbon column (Hypercarb, 2.1 mm, inner diameter × 100 mm, 3 μm, Thermo Fisher Scien-

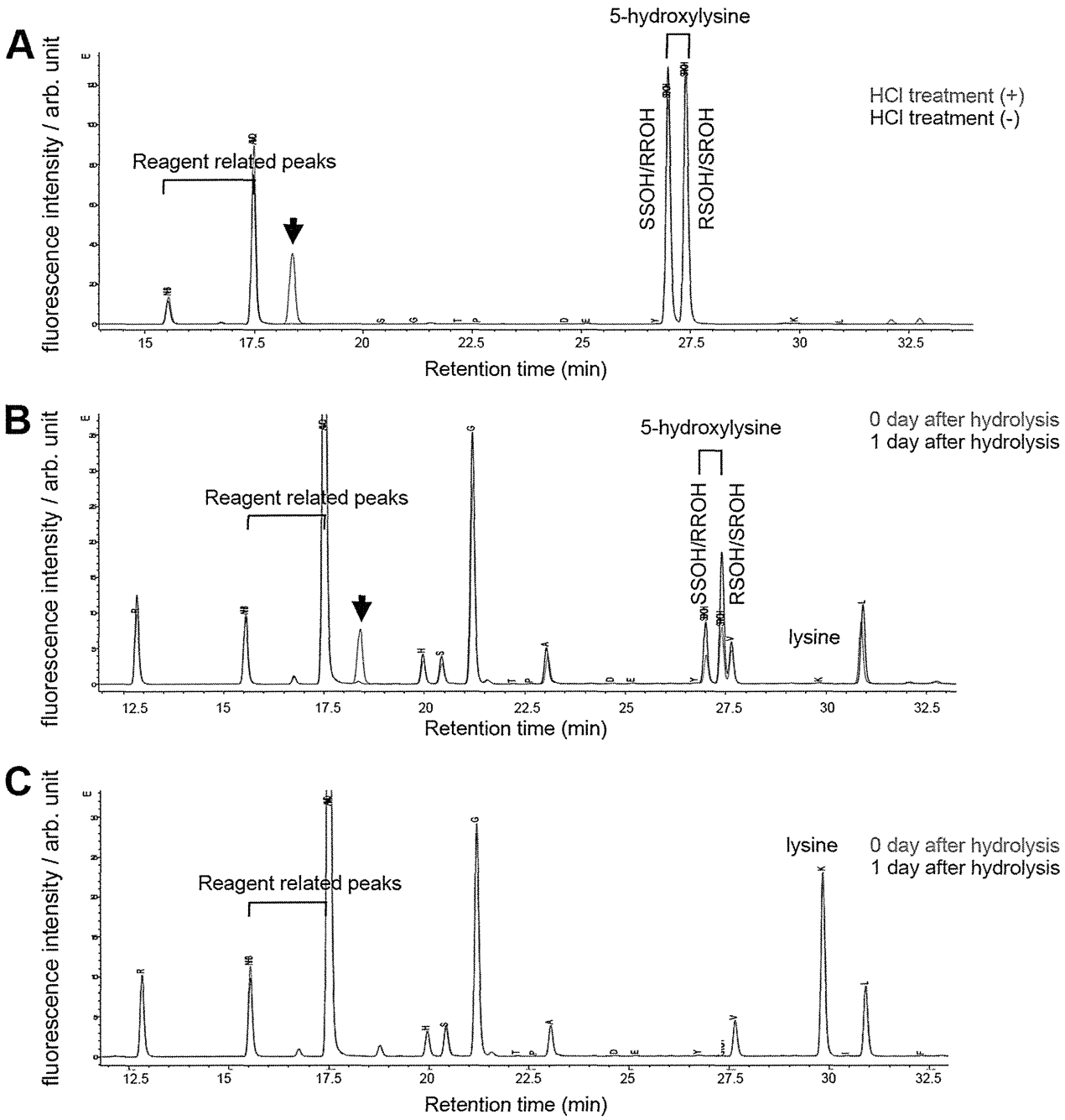

FIGURE 2. **Establishment of amino acid composition analysis for detecting 5-hydroxylysine.** *A*, analysis of simplicial synthetic SR-hydroxylysine and synthetic racemic mixture (*SS/RR/RS/SR*) of 5-hydroxylysine either treated with (*red*) or without (*blue*) HCl. *B* and *C*, analysis of $H4_{1-20}$ peptides including synthetic 5-hydroxylysine (*B*) and unmodified $H4_{1-20}$ peptides (*C*). The peptides were analyzed in the same day of hydrolysis (*red*) or next day of hydrolysis (*blue*). The *arrow* indicates a 5-hydroxylysine derived peak, which possibly corresponds to a lactone derivative, 3-amino-6-(aminomethyl)oxan-2-one. *SSOH/RROH*, 2*S*,5*S*-/2*R*,5*R*-hydroxylysine; *RSOH/SROH*, 2*R*,5*S*-/2*S*5*R*-hydroxylysine; *arb. unit*, arbitrary units.

tific, Inc., Waltham, USA), and a fraction including 5-hydroxylysine was derivatized with 6-aminoquinolylcarbamyl. The 6-aminoquinolylcarbamyl amino acids were separated on a C18-reversed phase column (Inertsustain C18HP, 3.0 mm, inner diameter × 250 mm, 3 μm, GL Sciences, Tokyo, Japan) and quantified. Synthetic racemic mixture of DL-5-hydroxylysine (catalog no. H0377, Sigma-Aldrich), and 2*S*,5*R*-hydroxylysine (catalog no. 55501, Sigma-Aldrich) were used as standards.

In Vitro Histone Acetyltransferase (HAT) Assay—The *in vitro* p300 colorimetric HAT assay was performed according to a protocol from BIOMOL (Plymouth Meeting, PA). In brief, the catalytic domain of human p300 (catalog no. SE-451, BIOMOL) and the indicated amount of control histone $H4_{1-23}$ peptides or 5-hydroxylysine containing histone $H4_{1-23}$ peptides, in which all lysines were substituted to 5-hydroxylysine (Sigma-Genosys, Hokkaido, Japan), were incubated in 50 μl of assay buffer (50 mM HEPES/NaOH (pH 7.9), 0.1 mM EDTA, 50 μg/ml BSA) in

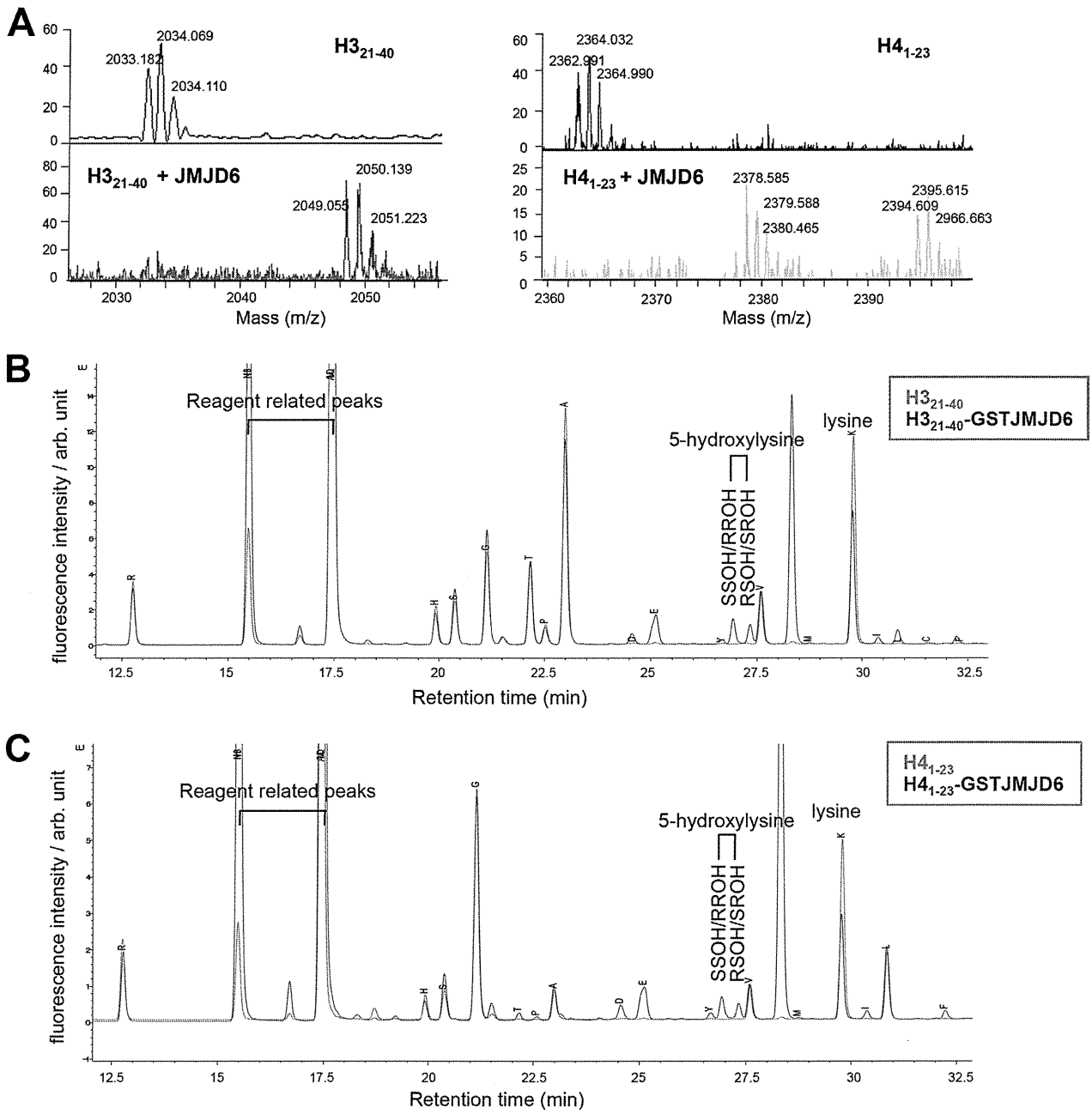

FIGURE 3. **JMJD6 hydroxylates histone H3 and H4 peptides detected by amino acid composition analysis.** *A*, hydroxylation of $H3_{21-40}$ and $H4_{1-23}$ peptides by GST-JMJD6 was confirmed by MS analysis. *B* and *C*, results of amino acid composition analysis of $H3_{21-40}$ (*B*) and $H4_{1-23}$ (*C*) peptides treated with (*blue*) or without (*red*) GST-JMJD6. *SSOH/RROH*, 2*S*,5*S*/2*R*,5*R*-hydroxylysine; *RSOH/SROH*, 2*R*,5*S*-/2*S*,5*R*-hydroxylysine; *arb. unit*, arbitrary units.

the presence of acetyl-coenzyme A (CoA, Sigma-Aldrich) at 37 °C. The reaction was stopped by adding 100 μl of quenching buffer (3.2 M guanidinium HCl, 100 mM Na_2HPO_4/NaH_2PO_4 (pH6.8)) at the indicated times. Following this, 50 μl of 2 mM 5,5′-dithiobis-2-nitrobenzoic acid (Sigma-Aldrich) in 100 mM Na_2HPO_4/NaH_2PO_4 (pH 6.8) was added, and absorbance at 405 nm was read by a spectrophotometer (ARVO MX/Light 1420 Multilabel/Luminescence Counter, PerkinElmer Life Sciences). The transfer of an acetyl group from an acetyl-CoA to the ϵ-amino group of lysine residues was quantified by measurement of the thiol group of CoA. A standard curve was generated using β2-mercaptoethanol.

In Vitro Histone Methyltransferase Assay—The *in vitro* histone methyltransferase assay was performed as described previously (10), except for slight modifications. In brief, a fixed amount of purified baculovirus-produced recombinant SMYD3 (1 μM) was incubated with indicated histone peptides, which were also used for the *in vitro* HAT assay, and 1 μCi of *S*-adenosyl-L-methionine (AdoMet; GE Healthcare) as the methyl donor in a mixture of 60 μl of methylase activity buffer (50 mM Tris-HCl (pH 8.5), 100 mM NaCl, 10 mM dithiothreitol) at 30 °C. The incorporated ^3H-labeled methyl groups in the substrates were measured by a scintillation counter after filter binding (units, cpm). The concentration

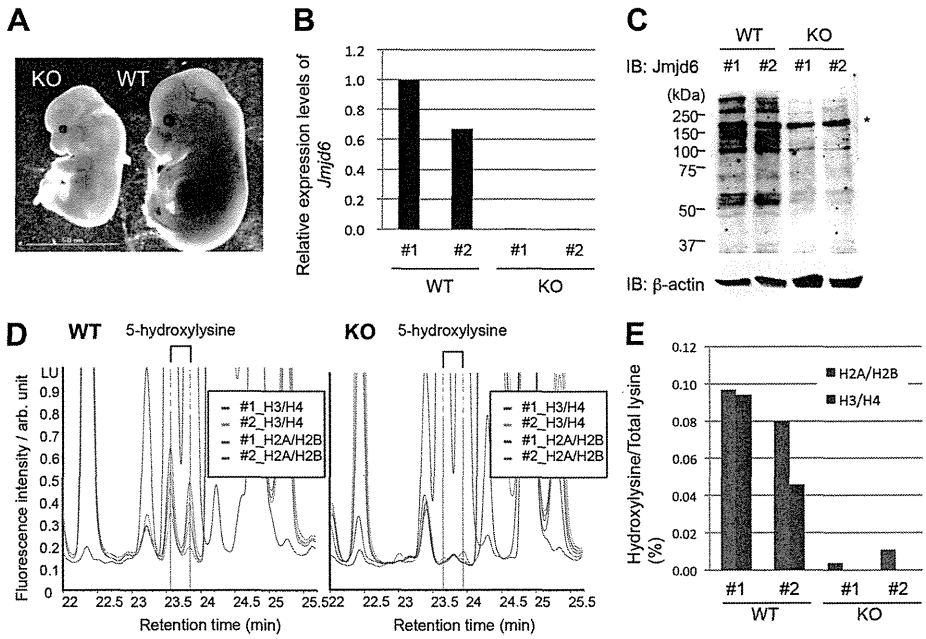

FIGURE 4. **JMJD6 hydroxylates histones H2A/H2B and H3/H4 in mouse embryos.** *A*, a representative image of JMJD6 knock-out and wild-type E14.5 embryos. *B*, *JMJD6* knock-out was confirmed by qRT-PCR. GAPDH was used as an internal control. *C*, JMJD6 knock-out was confirmed by Western blotting. The *asterisk* indicates a nonspecific band. β-Actin was used as a loading control. *D*, result of amino acid composition analysis of histones derived from two Jmjd6 wild-type (*left*) and knock-out (*right*) E14.5 embryos. *E*, % of 5-hydroxylysine in total lysine of histones H2A/H2B (*blue*) and H3/H4 (*red*) was calculated from the HPLC data (*D*). *IB*, immunoblot; *arb. unit*, arbitrary units.

(nM) of the methylated substrate was calculated based on the basis of radioactivity.

RESULTS

JMJD6 Effectively Hydroxylates Histone Lysyl Residues in Vitro—During screening of UHRF1-interacting proteins, we identified JMJD6 as a novel binding partner of UHRF1 (data not shown). Because UHRF1 recognizes hemimethylated DNA and histone modifications, we assumed that JMJD6 might be recruited by UHRF1 to nucleosomes and modify histone lysyl residues. *In vitro* experiments showed that recombinant GST-JMJD6 possessed the ability to bind to histone $H3_{1-20}$ tail and histone H4 (Fig. 1, *A* and *B*) and hydroxylate multiple lysyl residues in the N-terminal tails of histone $H3_{1-20}$ and $H4_{1-30}$, which was detected as of 16, 32, or 48 Da shifts by MS analysis (Fig. 1, *C* and *D*); subsequent MS/MS analysis revealed that JMJD6 mediates monohydroxylation of lysyl residues. As indicated by Webby *et al.* (1), JMJD6 preferentially hydroxylated lysyl residues in the basic peptides, and no apparent sequence preference was observed *in vitro* (data not shown).

Next, we established a sensitive hydroxylysine detection method based on amino acid composition analysis as an alternative to the MS-based method. For amino acid composition analysis, we briefly hydrolyzed peptides or proteins with HCl and separated each amino acid residue by reversed phase HPLC to detect 5-hydroxylysine. To evaluate this method, we first performed reversed phase HPLC using simplicial synthetic 2*S*,5*R*-hydroxylysine and synthetic racemic mixture of 5-hydroxylysine composed of 2*S*,5*S* (*SS*)-, 2*R*,5*R* (*RR*)-, 2*R*,5*S* (*RS*)-, and 2*S*,5*R* (*SR*)-stereoisomers (Fig. 2*A*). We detected two peaks corresponding to *SS*/*RR*- and *RS*/*SR*-hydroxylysine by analyzing these synthetic 5-hydroxylysines without HCl treatment (Fig. 2*A*). After HCl treatment of these synthetic 5-hydroxylysines, another peak was appeared (Fig. 2*A*, *arrow*). This peak possibly corresponds to a lactone derivative, 3-amino-6-(aminomethyl)oxan-2-one, generated by dehydration condensation between C5 hydroxyl group and carboxyl group, which is described in a previous report (11). Next, we evaluated the method using unmodified $H4_{1-23}$ peptides and 5-hydroxylysine containing $H4_{1-23}$ peptides in which all the lysines at positions 5, 8, 12, and 20 were substituted with 5-hydroxylysines. After hydrolysis of these peptides, we detected two peaks corresponding to *SS*/*RR*- and *RS*/*SR*-hydroxylysine only in the 5-hydroxylysine containing peptides but not in the unmodified peptides (Fig. 2, *B* and *C*). We also detected the peak of the possible lactone derivative in the 5-hydroxylysine containing peptides by reversed phase HPLC performed in the same day of hydrolysis, but the peak disappeared in the next day of hydrolysis, indicating that the derivative is unstable. Because quantification of the derivative is technically difficult, we only quantified *SS*/*RR*- and *RS*/*SR*-hydroxylysine.

Using this method, we analyzed $H3_{21-40}$ and $H4_{1-23}$ peptides treated with or without recombinant GST-JMJD6. First, we confirmed hydroxylation of the peptides by GST-JMJD6 by MS analysis (Fig. 3*A*). Then, the peptides were separated from the enzyme reaction mixture, by reversed phase HPLC. The separated peptides were treated with HCl, and each amino acid residue was separated by reversed phase HPLC (Fig. 3, *B* and *C*). Comparison of the chromatograph between amino acids derived from the JMJD6-treated and -untreated peptides identified two additional peaks in the peptides treated with JMJD6, which are matched with the standard synthetic 5-hydroxylysine (Fig. 3, *B* and *C*).

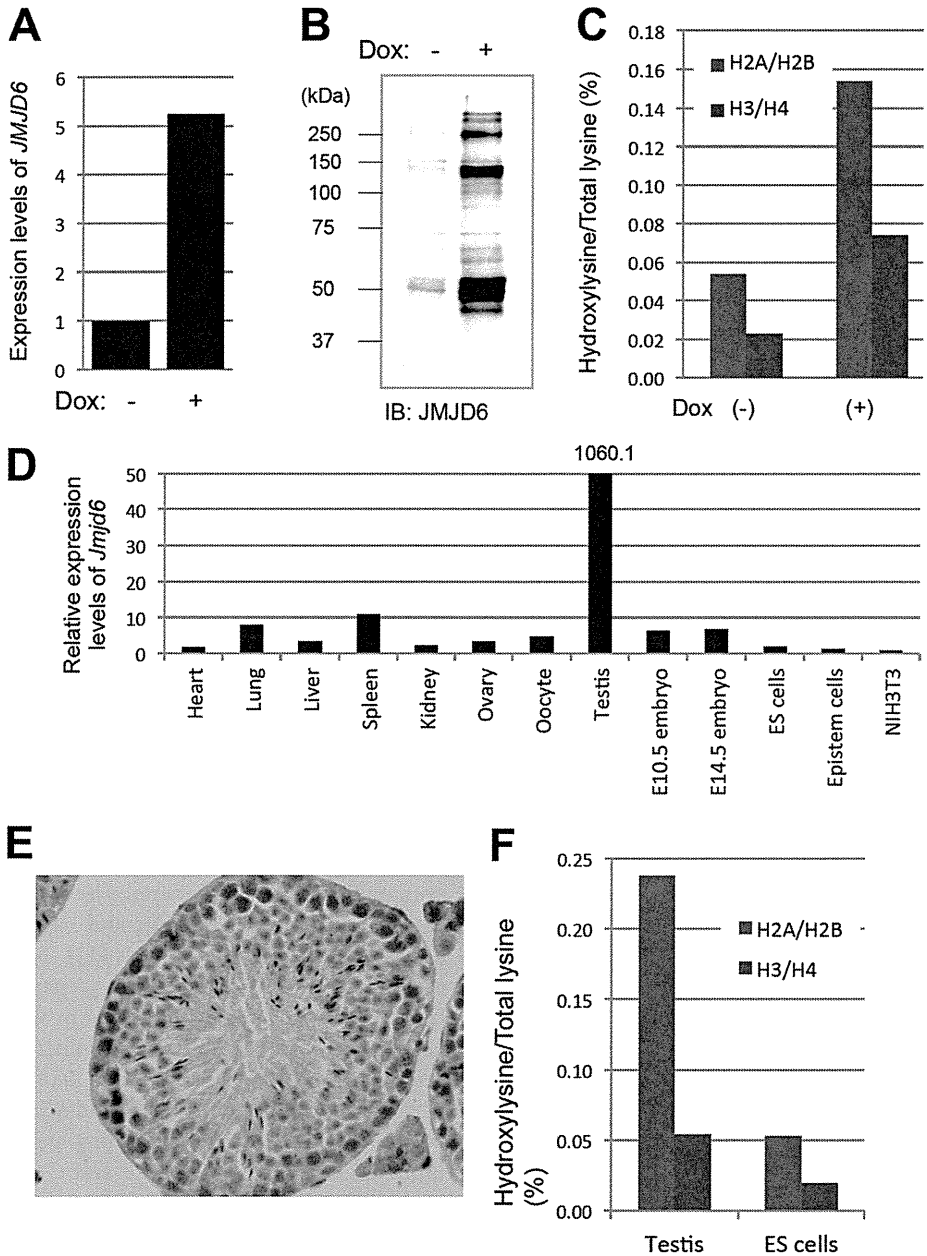

FIGURE 5. **Amount of 5-hydroxylysine in JMJD6 overexpressed HEK 293 cells, mouse testis, and ES cells.** *A*, expression levels of *JMJD6* in Dox-inducible JMJD6 stable cells were examined by qRT-PCR before and after 48-h Dox induction. *B*, induction of JMJD6 by Dox in the cells was confirmed by Western blotting. *C*, amino acid composition analysis of histones derived from Dox-inducible JMJD6 stable cell lines. The *blue* and *red bars* indicate % of 5-hydroxylysine in the total lysine of histone H2A/H2B and in the H3/H4, respectively. *D*, relative expression levels of *Jmjd6* in various mouse tissues and cells were examined by qRT-PCR. *E*, expression of Jmjd6 in a 6-month-old mouse testis was examined by immunohistochemistry. *F*, amino acid composition analysis of histones derived from 6-month-old mouse testis and J1 ES cells. The *blue* and *red bars* indicate % of 5-hydroxylysine in the total lysine of histone H2A/H2B and in the H3/H4, respectively.

JMJD6 Hydroxylates Histone Lysyl Residues in Vivo—To investigate histone lysyl hydroxylation *in vivo*, we performed the amino acid composition analysis for analyzing a mixture of histone H2A/H2B and a mixture of histone H3/H4 proteins isolated from two JMJD6 wild-type and two JMJD6 knock-out whole embryos at E14.5 (Fig. 4*A*). JMJD6 knock-out was confirmed by qRT-PCR and Western blotting (Fig. 4, *B* and *C*). The results showed that 0.097 and 0.080% of total lysyl residues in histone H2A/H2B and 0.094 and 0.046% of those in histone H3/H4 were 5-hydroxylated in each of the two JMJD6 wild-type mice (Fig. 4, *D* and *E*), whereas 0.004 and 0.011% of total lysyl residues in histone H2A/H2B and 0.000 and 0.000% of those in histone H3/H4 were 5-hydroxylated in each of the two JMJD6 knock-out mice (Fig. 4, *D* and *E*), indicating that JMJD6 hydroxylates histone lysyl residues *in vivo*.

We also generated Dox-inducible JMJD6 stable HEK293 cells. JMJD6 induction by Dox was confirmed by qRT-PCR and Western blotting (Fig. 5, *A* and *B*) and increased 5-hydroxylation levels of histone lysyl residues (Fig. 5*C*). In addition, we purified histones from a 6-month-old JMJD6 wild-type mouse

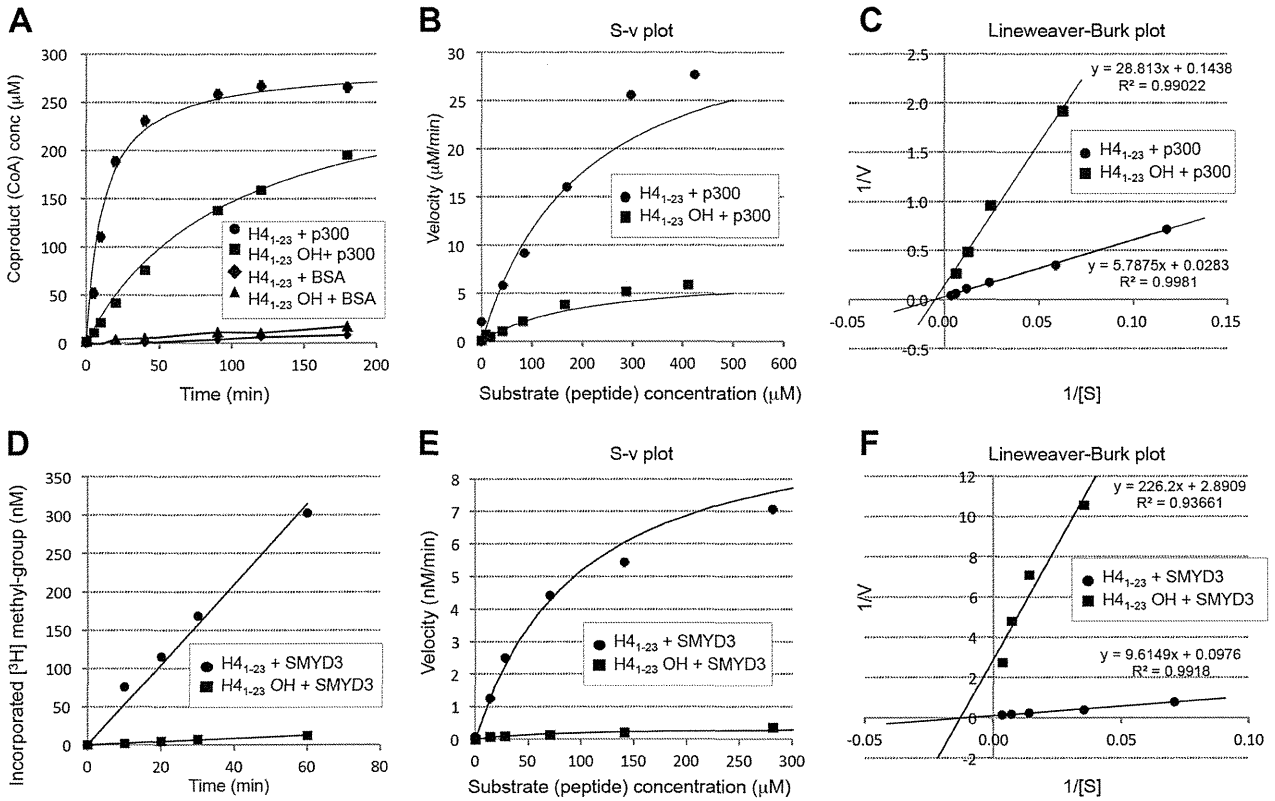

FIGURE 6. **5-Hydroxylation of lysyl residue impairs *N*-acetylation and *N*-methylation *in vitro*.** *A–C*, the *in vitro* colorimetric HAT assay was performed using a fixed amount of p300 (0.44 μM) and control H4$_{1-23}$ peptides (●) or 5-hydroxylysine-containing peptides (H4$_{1-23}$ OH, ■). BSA was used as a negative control (◆, ▲). After the reactions, absorbance (405 nm) of the coproduct (CoA) was measured. *A*, reactions were terminated at the indicated time points, and the concentration of CoA was calculated on the basis of a standard curve that was generated from β2-mercaptoethanol. *B* and *E*, substrate concentration-velocity (s-v) plot. *C* and *F*, Lineweaver-Burk plot. The *vertical axis* is 1/velocity [v], and the *horizontal axis* is 1/substrate concentration [S]. *D–F*, the *in vitro* histone methyltransferase assay was performed using a fixed amount of SMYD3 (1 μM) and control H4$_{1-23}$ peptides (●) or 5-hydroxylysine-containing peptides (H4$_{1-23}$OH, ■). AdoMet was used as a methyl donor. After the reactions, radioactivity (cpm) of the ^{3}H-methylated substrates was measured. The concentration of incorporated ^{3}H-methyl groups (nM) was calculated based on the basis of radioactivity (1 cpm was 0.02563 nM in the reaction). *D*, reactions were performed with fixed amounts of the peptides (141 μM) and terminated at the indicated time points.

testis, which expressed JMJD6 at the highest level among various tissues and cells (Fig. 5, *D* and *E*). In the testis, 0.238 and 0.054% of total lysyl residues in histone H2A/H2B and H3/H4, respectively, were 5-hydroxylated (Fig. 5*F*). In the mouse J1 ES cells, 0.053 and 0.020% of total lysyl residues in histone H2A/H2B and H3/H4, respectively, were 5-hydroxylated (Fig. 5*F*).

5-Hydroxylation Prevents N-Acetylation and N-Methylation of Histone Lysyl Residues in Vitro—Because lysyl residues in histone tails are often subjected to *N*-acetylation and *N*-methylation, we examined whether 5-hydroxylation of lysyl residues affects modifications at the ϵ-amino groups. First, we examined the effect of lysyl 5-hydroxylation on histone H4 *N*-acetylation by p300, which catalyzes *N*-acetylation of the ϵ-amino group of lysyl residues, including histone H4K5 and H4K8, through its HAT domain (12). Kinetic analysis using the unmodified and the 5-hydroxylysine containing H4$_{1-23}$ peptides in which all the lysines were substituted with 5-hydroxylysines as substrates revealed that 5-hydroxylation largely interfered with the HAT activity of p300 *in vitro* (Fig. 6, *A–C*). Lineweaver-Burk plot analysis was performed to calculate the maximum velocity (V_{max}) and Michaelis constant (K_m) values (Table 1; Fig. 6*C*, $R^2 = 0.9981$ and 0.9902). V_{max} of the reactions in which p300 acetylated the 5-hydroxylysine-containing peptides (H4$_{1-23}$OH) was 5-fold less than that of the control peptides (6.95 ± 0.45 and 35.34 ± 1.65 μM/min, respectively), whereas K_m of the two reactions was quite similar (204.51 ± 10.12 and 200.37 ± 14.32 μM, respectively), indicating that 5-hydroxylation does not inhibit binding of lysyl residues to p300 but reduces the catalytic efficiency.

TABLE 1

Effect of 5-hydroxylation on *N*-acetylation of ϵ-amino group of lysyl residues

Lineweaver-Burk plots were used for estimation of the kinetic constants, V_{max}, and K_m. R^2 is the determination coefficient (see Fig. 6*C*).

	V_{max}	K_m
	μM/min	*μM*
H4$_{1-23}$ + p300	35.34 ± 1.65 (R^2 = 0.9981)	204.51 ± 10.12
H4$_{1-23}$ OH + p300	6.95 ± 0.45 (R^2 = 0.9902)	200.37 ± 14.32

TABLE 2

Effect of 5-hydroxylation on *N*-methylation of ϵ-amino group of lysyl residues

Lineweaver-Burk plots were used for estimation of the kinetic constants, V_{max}, and K_m. R^2 is the determination coefficient (see Fig. 6*F*).

	V_{max}	K_m
	nM/min	
H4$_{1-23}$ + SMYD3	10.90 ± 0.92 (R^2 = 0.9918)	80.63 ± 16.26 μM
H4$_{1-23}$ OH + SMYD3	0.48 ± 0.26 (R^2 = 0.9366)	75.26 ± 9.60 μM